7. C. Zener, *Phys. Rev.* **82**, 403 (1951).
8. P.-G. de Gennes, *Phys. Rev.* **118**, 141 (1960).
9. P. W. Anderson, H. Hasegawa, *Phys. Rev.* **100**, 675 (1955).
10. A. J. Millis, P. B. Littlewood, B. I. Shraiman, *Phys. Rev. Lett.* **74**, 5144 (1995).
11. Y. Tokura, Ed., *Colossal Magnetoresistive Oxides*, vol. 2 of *Advances in Condensed Matter Science* (Gordon and Breach, Amsterdam, 2000).
12. Z. X. Shen, D. S. Dessau, *Phys. Rep.* **253**, 1 (1995).
13. The ARPES experiments were performed at undulator Beamline 10.0.1 at the ALS, using a Scienta SES 200 energy analyzer. All data shown here were taken with 50-eV photons at 20 K in a vacuum better than 4×10^{-11} torr. The angle mode of the analyzer was used, allowing us to simultaneously collect ~38 individual spectra along a ~12° angular slice in θ. The energy resolution of the analyzer was better than 10 meV, measured from the 10 to 90% width of the Au reference taken at 10 K, and the angular resolution was ±0.16° along the angular slice and ±0.25° in the perpendicular direction ϕ, giving a momentum resolution

$$(\Delta k_x, \Delta k_y) = \left(0.02\frac{\pi}{a}, 0.033\frac{\pi}{a}\right)$$

To grid the Brillouin zone, the samples were rotated in the ϕ direction in 1° steps. The analyzer was left fixed, with the central axis making an 83° angle relative to the photon beam. In this configuration, the 12° slices were parallel to the incident photon polarization direction, which was mostly out of plane.
14. The EDCs presented here were normalized with emission intensity in a binding energy (0.1 eV to 0.25 eV) on the unoccupied side of E_F. Such high-order harmonic emission is isotropic and is proportional to photon flux.
15. N. Hamada, unpublished data.
16. D. S. Dessau *et al.*, *Phys. Rev. Lett.* **81**, 192 (1998).
17. S. Massidda *et al.*, *Physica C* **152**, 251 (1988).
18. Y.-D. Chuang *et al.*, preprint available at http://xxx.lanl.gov/abs/cond-mat/0102386.
19. D. L. Feng *et al.*, preprint available at http://xxx.lanl.gov/abs/cond-mat/0102385.
20. T. Saitoh *et al.*, *Phys. Rev. B* **62**, 1039 (2000).
21. The FS centered around (0,0) will of course have very different parameters, but these will not be very relevant for the in-plane conductivity.
22. Qing An Li, K. E. Gray, J. F. Mitchell, *Phys. Rev. B* **63**, 24417 (2001).
23. A. Abrikosov, *Phys. Rev. B* **61**, 7770 (2000).
24. R. Joynt, *Science* **284**, 777 (1999).
25. D. S. Dessau, T. Saitoh, *Science* **287**, 767a (2000).
26. K. Schultz *et al.*, *Phys. Rev. B* **63**, 165429 (2001).
27. T. Ishikawa, T. Kimura, T. Katsufuji, Y. Tokura, *Phys. Rev. B* **57**, R8079 (1998).
28. T. Ishikawa, K. Tobe, T. Kimura, T. Katsufuji, Y. Tokura, *Phys. Rev. B* **62**, 12354 (2000).
29. A. J. Millis, B. I. Shraiman, R. Mueller, *Phys. Rev. Lett.* **77**, 175 (1996).
30. A. J. Millis, R. Mueller, B. I. Shraiman, *Phys. Rev. B* **54**, 5405 (1996).
31. D. J. Singh, W. E. Pickett, *Phys. Rev. B* **57**, 88 (1998).
32. H. Roder, J. Zang, A. I. Bishop, *Phys. Rev. Lett.* **76**, 1356 (1996).
33. A. S. Alexandrov, A. M. Bratkovsky, *Phys. Rev. Lett.* **82**, 141 (1999).
34. V. Ferrari, M. J. Rozenberg, R. Weht, preprint available at http://xxx.lanl.gov/abs/cond-mat/9906131.
35. A. Moreo, S. Yunoki, E. Dagotto, *Science* **283**, 2034 (1999).
36. A. Moreo, M. Mayr, A. Feiguin, S. Yunoki, E. Dagotto, *Phys. Rev. Lett.* **84**, 5568 (2000).
37. S. Mori *et al.*, *Nature* **392**, 473 (1998).
38. T. Hotta, A. Feiguin, E. Dagotto, *Phys. Rev. Lett.* **84**, 2477 (2000).
39. M. Mayr *et al.*, *Phys. Rev. Lett.* **86**, 135 (2001).
40. D. Argyriou *et al.*, *Phys. Rev. B* **61**, 15269 (2000).
41. X.-J. Zhou *et al.*, *Science* **286**, 268 (1999).
42. V. J. Emery, S. A. Kivelson, J. M. Tranquada, preprint available at http://xxx.lanl.gov/abs/cond-mat/9907228.
43. S. Shimomura, N. Wakabayashi, H. Kuwahara, Y. Tokura, *Phys. Rev. Lett.* **83**, 4389 (1999).

44. We thank D. Argyriou, B. Campbell, R. Osborn, E. Dagotto, J. Zhang, A. Fedorov, and N. Hamada for helpful discussions; S. Kellar, X. J. Zhou, P. Bogdanov, and Z. Hussain for instrumentation help; and J. Denlinger for analysis software. Supported by NSF grant CAREER-DMR-9985492 and U.S. Department of Energy (DOE) grant DOE DE-FG03-00ER45809. ALS is supported by DOE.

23 January 2001; accepted 10 April 2001
Published online 26 April 2001;
10.1126/science.1059255
Include this information when citing this paper.

Evidence for a Solar System–Size Accretion Disk Around the Massive Protostar G192.16–3.82

D. S. Shepherd,[1*] M. J. Claussen,[1] S. E. Kurtz[2]

Seven-millimeter continuum observations of a massive bipolar outflow source, G192.16–3.82, were made at a milli–arc-second resolution with a capability that links the National Radio Astronomy Observatory's Very Large Array radio interferometer with the Very Long Baseline Array antenna, located in Pie Town, New Mexico. The observations provide evidence for a true accretion disk that is about the size of our solar system and located around a massive star. A model of the radio emission suggests the presence of a binary protostellar system. The primary protostar, G192 S1, at the center of the outflow, with a protostar mass of about 8 to 10 times the solar mass, is surrounded by an accretion disk with a diameter of 130 astronomical units (AU). The mass of the disk is on the order of the protostar mass. The outflow is poorly collimated with a full opening angle of about 40 degrees; there is no indication of a more highly collimated jetlike component. The companion source, G192 S2, is located 80 AU north of the primary source.

During the early phases of stellar formation, central protostars are surrounded by a flattened rotating disk of dust and gas. This accretion disk may serve several critical functions: (i) it allows material to accrete onto the central star, thus building up the mass of the star over time; (ii) it powers energetic bipolar outflows that carry away mass and angular momentum; and (iii) toward the latter phase of the accretion process, the disk remnant provides the raw materials necessary for building planetary systems (*1–4*). The characterization of the region of the disk that powers outflow and accretion, as well as the geometry and energetics of the flow when it is first ejected from the protostellar system and collimated, is critical to our understanding of early star and planet formation processes. This avenue of research is already well-advanced for low-luminosity protostars, which will eventually evolve into a star like our Sun and which may form planetary systems similar to our own (*5*). The study of more luminous, and hence more massive, protostellar systems [$L_\star > 1000\ L_\odot$ and $M_\star > 5\ M_\odot$ ($L_\star$, protostar luminosity; $L_\odot$, solar luminosity; $M_\star$, protostar mass; $M_\odot$, solar mass)] is more difficult because there are fewer luminous stars than low-luminosity stars, they tend to form in compact clusters that generally lie more than a kiloparsec (1 kpc ≈ 3260 light years) away, and they can spend their entire protostellar lifetime obscured within dense molecular clouds. Yet, to advance our understanding of the formation process of stars of all luminosities, we must detail the physical conditions associated with luminous protostars, their accretion disks, and their outflows.

G192.16–3.82 (IRAS 05553+1631, hereafter G192.16) is a massive protostellar system. At a distance of ~2 kpc, G192.16 has a luminosity of $\sim 3 \times 10^3\ L_\odot$, which implies the presence of an early B star with a mass of 8 to 10 $M_\odot$ (*6, 7*). A high-velocity CO outflow with a roughly east-west orientation and an infrared reflection nebula are centered on the massive protostar (*7–10*). The outflow

[1]National Radio Astronomy Observatory, Post Office Box 0, Socorro, NM 87801, USA. [2]Instituto de Astronomía, Universidad Nacional Autónoma de México, Apartado Postal 70-264, C.P. 04510 México D.F., México.

*To whom correspondence should be addressed. E-mail: dshepher@aoc.nrao.edu

($M_{flow} = 95\ M_{\odot}$, dynamical age of $\sim 1.7 \times 10^5$ years) has emerged from the 500 $M_{\odot}$ molecular core (7, 10). Beyond the area of CO emission, high-surface-brightness Herbig-Haro objects are located more than 5 pc from the protostar, making this one of the longest and most spatially extended outflows in the Milky Way Galaxy (11).

On a smaller scale, there is evidence for an ionized outflow with an opening angle of ~50° based on a 0.5″ resolution centimeter continuum emission image (10). A lower luminosity protostar, located ~500 astronomical units (AU) north of G192.16, appears to be powering a jet with mixed synchrotron and thermal emission. The cloud core is associated with variable 22-GHz H_2O maser emission that appears to arise from a flattened rotating structure centered on G192.16, with a diameter of ~1000 AU (10, 12). Based on comparisons with outflow and accretion models developed for low-mass protostars, the diameter of this disklike structure is larger than the expected size of an accretion disk that could produce such a powerful outflow (1, 2, 13–15). Using the dynamical argument to equate the outflow kinetic energy with the gravitational potential energy, we found that the disk radius at which the outflow is ejected is $2GM_{\star}/v_w^2$, where G is the gravitational constant and v_w is the wind velocity. For a 10 $M_{\odot}$ star like G192.16, assuming an initial outflow velocity of 100 to 1000 km s^{-1}, the radius at which the outflow must be ejected is ~2 to 0.02 AU. This is about the same size scale required to launch the observed 100 km s^{-1} jets in low-mass protostellar systems. Therefore, the 1000-AU structure detected in G192.16 is probably not directly powering the outflow, but it may be a rotating torus or an extension of the inner accretion disk. At a distance of 2 kpc, 10 milli–arc sec (mas) corresponds to 20 AU; thus, to image the G192.16 circumstellar region where the outflow is expected to be generated, milli–arc-second resolution is required.

Observations at 43.34 GHz were made with the Very Large Array (VLA) linked with the Very Long Baseline Array's (VLBA) Pie Town (PT) antenna by a real-time fiber-optic connection (16). The VLA was in its most extended configuration (A array) with a maximum baseline length of 36.4 km. The PT antenna is situated 52 km away from the center of the VLA. Continuum observations with 23 antennas were carried out on 24 November 2000 between 0600:00 and 1200:00 UT. A total bandwidth of 200 MHz was centered at 43.3399 GHz (Table 1). Using a method of fast switching between the source and gain calibrator, we tracked tropospheric phase variations of the atmosphere across the array (17). The milli–arc-second resolution resolved out ~10% of the total flux density. Therefore, A- and C-array data (10) were combined and imaged with a 30-mas full width at half maximum Gaussian taper to determine the structure of the more extended emission.

In the image from the VLA A array linked with the PT antenna (Fig. 1, right), a single elongated structure is detected at a resolution of 40 mas by 30 mas. The emission peak is located at the center of the G192.16 molecular outflow at position α(J2000) $5^h58^m13.53^s$ δ(J2000) 16°31′58.29″. The position angle of the structure is 17°. A bulge near the peak extends in an east-west direction, whereas the northern part of the emission remains relatively narrow. The image resulting from the combined A- and C-array data recovers all flux density previously detected (Fig. 1, left) (10). However, the resolution is not adequate to see detailed structure within the source. All 7-mm continuum emission is located within 0.08″ (160 AU) of the central protostar. No other extended emission was detected.

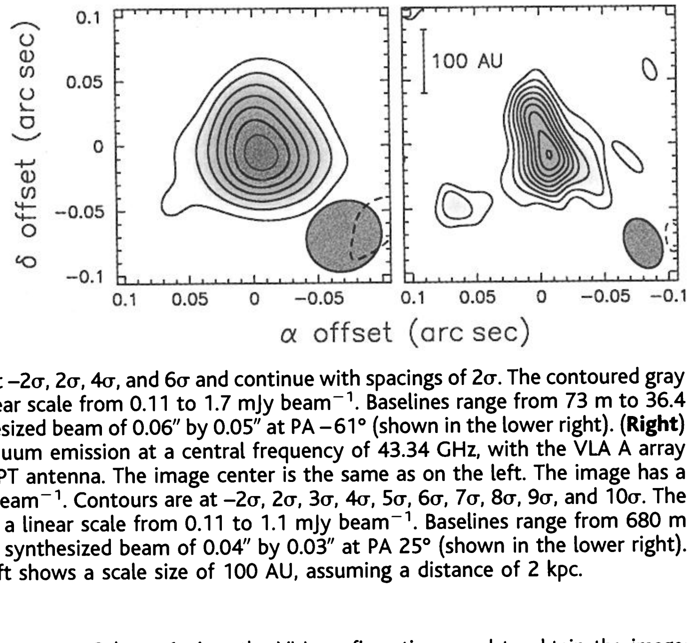

Fig. 1. Seven-millimeter continuum emission in G192.16–3.82. **(Left)** Seven-millimeter continuum emission at a central frequency of 43.34 GHz, with data from the VLA A and C arrays only. The image center (0, 0) is at position α(J2000) $5^h58^m13.530^s$ δ(J2000) 16°31′58.30″. The image has a rms noise of 0.11 mJy beam^{-1}. Contours are at −2σ, 2σ, 4σ, and 6σ and continue with spacings of 2σ. The contoured gray scale is plotted on a linear scale from 0.11 to 1.7 mJy beam^{-1}. Baselines range from 73 m to 36.4 km, resulting in a synthesized beam of 0.06″ by 0.05″ at PA −61° (shown in the lower right). **(Right)** Seven-millimeter continuum emission at a central frequency of 43.34 GHz, with the VLA A array linked with the VLBA's PT antenna. The image center is the same as on the left. The image has a rms noise of 0.11 mJy beam^{-1}. Contours are at −2σ, 2σ, 3σ, 4σ, 5σ, 6σ, 7σ, 8σ, 9σ, and 10σ. The gray scale is plotted on a linear scale from 0.11 to 1.1 mJy beam^{-1}. Baselines range from 680 m to 52 km, resulting in a synthesized beam of 0.04″ by 0.03″ at PA 25° (shown in the lower right). The bar in the upper left shows a scale size of 100 AU, assuming a distance of 2 kpc.

Table 1. Observational summary. Column 1 gives the VLA configurations used to obtain the image; columns 2 and 3 give the image resolution in terms of the full width at half maximum (FWHM) and position angle (PA), respectively, of the image beam; column 4 provides the measured root-mean-square (rms) noise in the image; and columns 5 and 6 give the peak and total flux density S_{ν}, respectively, in each image.

Continuum image	Beam FWHM	Beam PA	rms (mJy beam^{-1})	Peak S_{ν} (mJy beam^{-1})	Total S_{ν} (mJy)
A array and PT*	0.04″ by 0.03″	25.2°	0.11	1.1	2.74
C and A arrays†	0.06″ by 0.05″	−61.4°	0.11	1.7	3.05

*Highest resolution (10% of the extended emission has been resolved out). †Data from this and previous work (10) combined to recover extended emission.

For the creation of an accurate model of the emission in Fig. 1, right, a good initial estimate of the model components is necessary. Assuming a constant spectral index between 3.6 cm and 7 mm of 0.5 ± 0.1, ~75% of the detected 7-mm continuum flux density is likely due to ionized gas and the remaining ~25% is due to thermal dust emission (10). This estimate is very uncertain because only two continuum points were used to calculate the spectral index; however, it does give an idea of what to expect in terms of the relative contributions from ionized gas and dust emission. The ionized outflow has an east-west orientation that roughly matches the orientation of the larger scale CO and visible outflow (7, 11). Using a simple model of the expected emission from an ionized biconical outflow, we predict that the outflow opening angle is ~50° (10). The estimated inclination angle of the outflow is ~60° ± 10° (measured with respect to the line of sight) (7). Although we do not detect the 1000-AU-diameter torus in 7-mm continuum emission, we do detect a 200-AU structure at the peak of the 3.6-cm emission with a similar north-south orientation. The elongation of the emission is consistent with the presence of a compact disk centered on the protostar. Assuming that the disk is not precessing by more than a few degrees, we expect the inclination angle of the disk to be between 50° and 70°. Our initial model of the 7-mm emission is consistent with these predictions from previous observations and includes a central protostar surrounded by ionized gas and an ionized biconical outflow oriented approximately east-west. We assume that the thermal dust emission at 7 mm is produced in an accretion disk that is oriented roughly perpendicular to the observed large-scale outflow. The model disk is centered on the G192.16 protostar with the plane of the disk oriented perpendicular to the outflow.

To obtain the best fit of the model to the observations, we varied the location, size, flux density, and intensity distribution of the model components. The total intensity distribution from each model configuration was then convolved with a beam of 0.04″ by 0.03″ at a position angle of 25.2°, and the resulting convolved image was subtracted from the observed image to create a residual image. The model parameters were varied until the convolved model image matched the observed image as closely as possible. The top panel of Fig. 2A represents the best model that could be obtained with the protostar, disk, and outflow components defined above. With this three-component model, the only way to create an asymmetric northern extension of the 7-mm continuum emission is to offset the center of the disk from the protostar position. Even when this is done, the residual image shows that the model underestimates the flux density by $\sim 3\sigma$ north of the peak.

Thus, to fit the northern extension in the data, we added another source with an offset of ~80 AU from the emission peak. Again, the model parameters were varied until the best fit residual image was obtained (Fig. 2B and Table 2). The southern outflow source is named G192 S1, and the northern compact source is G192 S2 (Table 2). Above the 3σ contour level (Fig. 2), the model fits the source intensity distribution to within 0.5σ, except at the southern boundary. This excess observed emission in the south could be due to any number of physically plausible mechanisms, e.g., edge brightening in the outflow cavity due to warm dust or free-free emission, asymmetry in the outflow orientation, or, perhaps, clumpy molecular material in the disk. Because of a lack of information about the expected geometry of this emission, we did not attempt to model these components.

The best fit model outflow cone originates within 20 AU of G192 S1. The position angles of the G192 S1 disk and outflow cone can vary by up to ±5°, and the outflow cone opening angle can range from 30° to 50° and still fit the observations equally well. The final size of the best fit disk is 65 mas by 20 mas. Assuming circular symmetry of the disk, this corresponds to an inclination angle of 20° measured with respect to the line of sight. The perpendicular axis of the disk plane is within 10° of the estimated inclination angle of the large-scale CO outflow (~60°). The position angle of the best fit model outflow cone differs from that of the large-scale outflow by ~25°. A difference in position angle between the large- and small-scale components of an outflow is common in outflow-disk systems. One cause for differences greater than ~10° may be the precession of the disk, and hence the outflow (*18–20*). Precession could be caused by an interaction with a close binary companion, such as appears to be the case with the IRAS 20126+4014 outflow (*21*).

The details of the model components in G192 S2 are more uncertain. A central Gaussian emission peak plus uniform disk provides only marginal improvement in the fit over a single uniform disk or a single Gaussian source. The strongest constraints provided by the model are that the source must be ≲10 mas (20 AU) in diameter with a

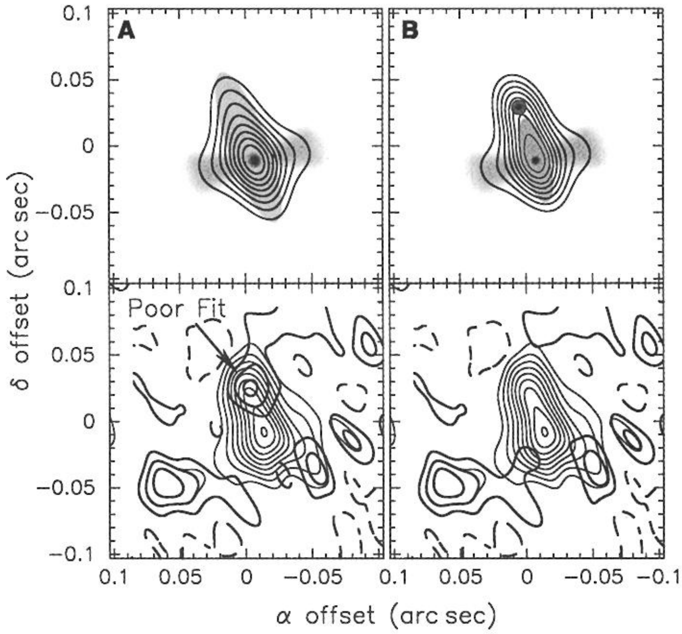

Fig. 2. Model fits to the data. (**A**) The top panel shows the best three-component model plotted with a linear gray scale from 0 to a peak flux density of 1.1 mJy beam^{-1}. The image center is the same as in Fig. 1. The model image convolved with a beam of 0.04″ by 0.03″ at PA 25.2° is shown in contours plotted at the same levels as in Fig. 1. The bottom panel shows the residual model image in thick contours plotted at −2 × 0.11, −1 × 0.11, 1 × 0.11, 2 × 0.11, 3 × 0.11, and 4 × 0.11 mJy beam^{-1} (the rms level in Fig. 1). Thin contours show the image of the VLA A array linked with the PT antenna (from Fig. 1, right) for comparison. The model underestimates the flux density by 2σ in the southwest. It also underestimates the flux density north of the peak by 3σ, even when the disk component is offset north of the primary source to produce an asymmetric extension. (**B**) The top panel shows the best model that now includes a compact companion located 80 AU from the central Gaussian peak. A gray scale is plotted on a linear scale from 0 to a peak flux density of 1.1 mJy beam^{-1}. The model image convolved with a beam of 0.04″ by 0.03″ at PA 25.2° is shown in contours plotted at the same levels as in Fig. 1. The bottom panel shows the residual model image in thick contours plotted at −2 × 0.11, −1 × 0.11, 1 × 0.11, 2 × 0.11, 3 × 0.11, and 4 × 0.11 mJy beam^{-1}. Thin contours show the image of the VLA A array linked with the PT antenna (from Fig. 1, right) for comparison. The model still underestimates the flux density by up to 2σ in the south; however, the bulk of the emission is now well fit by the model.

Table 2. Best fit model components for the G192 S1 and G192 S2 sources. Column 1 lists the types of emission component distributions used to construct the model; column 2 specifies the geometry of each component; columns 3 and 4, respectively, provide the peak and total flux density (the total flux density S_ν = 2.74 mJy in all model components); and column 5 gives the position of each component in terms of an offset from a central coordinate.

Component	Geometry	Peak S_ν (μJy)	Total S_ν (mJy)	Offset position from $5^h58^m13.530^s$ 16°31′58.29″ (mas)
	G192 S1			
Gaussian	3 mas (FWHM)	115.0	0.29	(0, 0)
Uniform disk	65 mas by 20 mas; PA 15° ± 5°	4.0	1.08	(0, 0)
Outflow cone*	PA 105° ± 5°; L = 46 mas; Θ_{open} = 40° ± 10°	4.4	0.73	(0, 0)
	G192 S2			
Gaussian	2 mas (FWHM)	210.0	0.23	(13, 40)
Uniform disk	10-mas diameter	20.0	0.41	(13, 40)

*Θ_{open} is the full opening angle of the cone; L is the distance from the protostar to the cone terminus.

total flux density of ~0.6 mJy (1 Jy = 10^{-26} W m^{-2} Hz^{-1}). The G192 S2 source is probably not a prestellar core because it is smaller than what is expected for such objects. The diameter of a prestellar core ranges from 2000 to 4000 AU (*22*), whereas the G192 S2 source is only 20 AU in diameter. It is improbable that such a compact core could avoid gravitational collapse. Thus, it is more likely that the G192 S2 source represents a binary companion to G192 S1. Assuming that the two sources are coeval, we predict that G192 S2 probably contains a protostar with a circumstellar envelope and/or disk.

In the remainder of this paper, we assume that the emission from the disk is mostly due to thermal dust emission and the emission in the central peak and outflow cone is due to ionized gas. These assumptions, although consistent with previous observations (*10*) and current theoretical understanding of outflow and accretion, may not be appropriate. In particular, the outflow may include warm dust heated by the interaction between the outflowing gas and the surrounding molecular cloud, and the disk may be partially ionized by stellar radiation and accretion shocks (*4*). Based on the model components (Table 2) and the above assumptions about the location of dust and ionized gas emission, an estimate of the physical properties of the G192.16 components can be made. Following the method of Hildebrand (*23*), we can estimate the mass of molecular material in the disk from the thermal dust emission using $M_{\mathrm{gas+dust}} = S_\nu D^2/B_\nu(T_d)\kappa_\nu$, where D is the distance to the source (2 kpc), S_ν is the continuum flux density due to thermal dust emission at frequency ν, and B_ν is the Planck function at dust temperature T_d. Assuming a gas-to-dust ratio of 100, the dust opacity per gram of gas is taken to be $\kappa_\nu = 0.006[\nu/(245\ \mathrm{GHz})]^\beta\ \mathrm{cm^2\ g^{-1}}$, where β is the opacity index (*24*). The mass estimate is dependent on the value chosen for the dust opacity index β and the characteristic dust temperature T_d. Shepherd *et al.* (*7*) find that $\beta = 1.5$ and $T_d = 40$ K for the warm molecular core and disk in G192.16. The disk itself is probably warmer than 40 K: A disk with an accretion rate of ~10^{-5} $M_\odot$ $\mathrm{year^{-1}}$ is expected to have a midplane temperature closer to 100 K at a radius of 30 to 50 AU (*25*). The opacity index $\beta = 1.5$ appears to be appropriate between wavelengths of 650 μm and 2.7 mm for submicrometer- to millimeter-sized grains expected in warm molecular clouds and young disks (*26*). However, fits to submillimeter and millimeter continuum emission find average values of $\beta \approx 1$ (*27*). For the G192 S1 accretion disk, the calculated mass ranges from 3 $M_\odot$ ($\beta = 1$ and $T_d = 100$) to an upper limit of 20 $M_\odot$ ($\beta = 1.5$ and $T_d = 40$). The disk mass could be lower than 3 $M_\odot$ if the emission is partially due to ionized gas. Despite the uncertainties associated with this estimate, the calculations above illustrate that the accretion disk surrounding G192 S1 has a mass of at least a few solar masses with disk mass $M_d \sim M_*$. The corresponding brightness temperature of the disk is ~200 K.

To estimate the spectral type of G192 S1, we assume that the emission in the outflow cone and the central peak is due to ionizing radiation from the central star. The number of Lyman continuum photons required to produce this emission is log N_L = 44.46 photons $\mathrm{s^{-1}}$, which corresponds to a single zero-age main-sequence B2 star with bolometric luminosity $L_{\mathrm{bol}} \sim 2.8 \times 10^3\ L_\odot$ (*28, 29*). There are several errors associated with this estimate. First, it assumes a spherically symmetric, homogeneous, ionization-bounded HII region, which is clearly not valid for this source, given that the ionized gas will be free to escape along the outflow axis. Second, there is no correction for dust absorption within the ionized gas, which would tend to underestimate N_L, and hence L_{bol}. Third, shock waves within the outflow are expected to contribute to the total ionizing flux, which would result in an overestimate of N_L. Despite these uncertainties, the estimate is probably accurate to within a single spectral type. Our calculations agree with those derived from the total ionizing radiation at 3.6 cm (*10*), which indicates that most of the ionizing radiation in this system is localized near G192 S1.

Because stars later than spectral type B3 would not produce an HII region detectable by our observations (*30*), our result suggests that the companion protostar, G192 S2, probably has a spectral type later than B3. This conclusion is supported by studies showing that millimeter flux is proportional to the bolometric luminosity of the embedded protostar (*31*). Thus, the lower 7-mm continuum emission of G192 S2 supports the interpretation that it is less luminous than G192 S1. If the flux density in the G192 S2 component is due mostly to thermal dust emission, an upper limit to the mass is 12 $M_\odot$. Assuming a total flux density of 0.6 mJy within a circular region 10 mas in diameter, the corresponding brightness temperature is <1500 K.

The H_2O masers in G192.16 (*10*) cover a much larger region (1000 AU) than the 200-AU region surrounding G192 S1 and G192 S2 (Fig. 1). It may be possible that the H_2O masers arise in the surface layers of a circumbinary disk or torus that was not detectable in our observations or in previous observations. On the basis of models and observations of disks in low-mass systems, we expect that a circumbinary disk or torus would be geometrically thick (*32, 33*). Although the density in the midplane of a self-gravitating disk should remain high, the midplane temperature is expected to decrease with increasing radius from the central source (*34*). Thus, if a circumbinary torus is present, the bulk of this high-density, cold gas would probably remain below our detection limit in 7-mm continuum emission (*35*). With the assumption that the

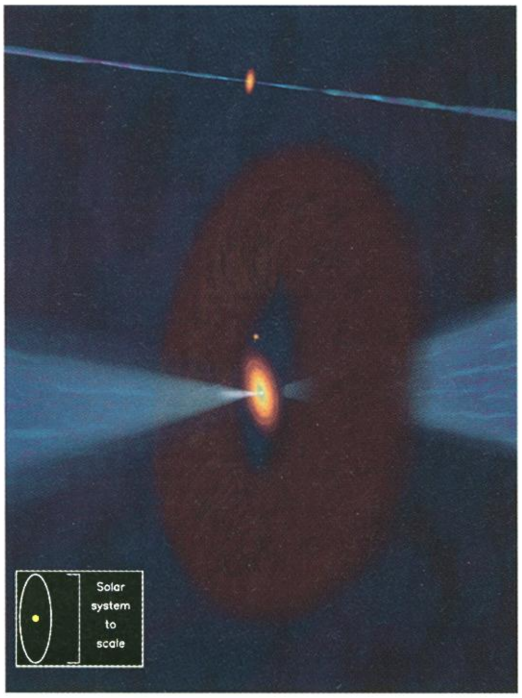

Fig. 3. An artist's conception of the possible geometry of the G192.16 protostellar system. North is up. The G192 S1 protostar is shown surrounded by a 130-AU-diameter accretion disk with a wide-angle outflow emanating from the central disk region. The G192 S2 companion is located 80 AU north of the primary S1 protostar. Near the northern edge of the circumbinary torus, a lower mass protostar with a well-collimated jet is shown. The actual location of this protostar and its associated disk is unknown because it has not been detected. However, the collimated jet and H_2O masers along the jet axis have been detected (*10*). Thus, the artist's rendition shows the protostar located somewhere along the observed jet axis. This drawing illustrates the dramatic difference between a typical jet outflow from a low-luminosity protostar that will become a star like our Sun (top of the image) and the outflow and accretion system of the massive protostar G192 S1. A scaled size of our solar system showing the 80-AU-diameter orbit of Pluto is in the bottom left. [Illustration: B. Starosta, NRAO/AUI/NSF]

H_2O masers trace a 1000-AU circumbinary torus, Fig. 3 presents an artist's conception of the possible geometry of this hierarchical triple system of a close binary pair with a third, more remote, star beyond the circumbinary disk. The accretion disk around G192 S1 may be affected by the binary companion, G192 S2. In a study of low-luminosity, multiple protostellar systems, hierarchical triples are common, and the dynamical decay of such systems may lead to strong outflow activity and disk truncation (*36*). The presence of a close binary companion may also tend to limit the accretion disk mass, and it can produce tidal forces that act to distort the disk and cause it to precess (*3, 4, 20, 21, 37, 38*).

The 130-AU accretion disk centered on G192 S1 is about the size of the disks detected around low-luminosity protostars; yet with a disk mass $M_d \sim M_\star$, the mass in the G192 S1 disk is 10 to 100 times that typically found in disks around T Tauri stars (*39*). Theory predicts that gravitational instabilities that induce spiral density waves will be prevalent in accretion disks with $M_d \gtrsim 0.3\ M_\star$ (*40, 41*). Thus, the massive G192 S1 disk may be denser and more turbulent than accretion disks around low-luminosity protostars. A measure of the stability of the disk can be obtained by calculating the Toomre Q parameter (*42*)

$$Q \equiv \frac{c_s\Omega}{\pi G\Sigma} = 56\left(\frac{M_\star}{M_\odot}\right)^{\frac{1}{2}}\left(\frac{R_d}{\mathrm{AU}}\right)^{-\frac{3}{2}} \times \left(\frac{T_d}{100\ \mathrm{K}}\right)^{\frac{1}{2}}\left(\frac{\Sigma}{10^3\ \mathrm{g\ cm^{-2}}}\right) \quad (1)$$

where c_s is the local sound speed, $\Omega = (GM_\star/r^3)^{1/2}$ is the epicycle frequency of the disk, $\Sigma = M_d/\pi R_d^2$ is the surface density of the disk, R_d is the disk radius, and T_d is the disk temperature. When Q drops below 1, the disk becomes susceptible to local gravitational instability and axisymmetric fragmentation. For the G192 S1 parameters of $M_\star = 8\ M_\odot$, $T_d = 100$ K, $R_d = 70$ AU, and $M_d = 3\ M_\odot$, $Q \sim 0.5$, indicating that the disk is locally unstable. However, this calculation is very uncertain because of the inherent uncertainty in our estimate of the disk temperature and mass.

Another implication of this work results from the estimate of the full opening angle in the G192 S1 outflow, $\Theta_{open} \sim 40°$. To our knowledge, estimates of the opening angle within 100 AU of the protostar have been made for three other massive outflows that are actively accreting material: (i) IRAS 20126+4104, $\Theta_{open} \sim 50° \pm 10°$ (*43, 44*); (ii) Cep A HW2, $\Theta_{open} \sim 15°$ within 1000 AU of the protostar (*45*), which increases to $\Theta_{open} \sim 60°$ beyond 0.1 pc from the source (*46*); and (iii) HH 80–81, $\Theta_{open} \sim 30° \pm 10°$ (*47*). In contrast, Hubble Space Telescope observations of jets from low-luminosity protostars indicate that the initial full opening angles are typically 20° to 40° but the opening angle narrows to only a few degrees within ~150 AU from the protostar (*48*). In disk-wind theory, as the outflow accelerates away from the disk into the far field, the hoop stress of the toroidal field component forces the outflow to self-collimate toward the rotation axis, forming a jet (*1*). The IRAS 20126, Cep A HW2, and G192 S1 massive outflows, all powered by early B–type protostars, have initial opening angles that are similar to the widest found in low-mass outflows, and they remain poorly collimated at large distances (0.1 to >1 pc) from the central source. One explanation for this could be that tidally induced precession of the disk, and hence the outflow, may help to widen the opening angle of the outflow cone. Another possibility is that outflows from more luminous stars may tend to be inherently less collimated. Support for this speculation comes from numerical simulations of magnetohydrodynamic disk winds from Keplerian accretion disks (*49*), which suggest that the mass load in the outflow wind controls the interplay between the collimating effects of the toroidal field and the kinetic energy density in the outflow. Thus, it is possible that the higher accretion and mass outflow rates in more luminous protostars may tend to inhibit the outflow collimation process. However, HH 80–81 is well-collimated for several parsecs, which indicates that there are conditions under which a luminous protostar can sustain a well-collimated, jetlike outflow. For a determination of whether poor outflow collimation is an inherent property of luminous protostars with high mass loads in the wind, additional massive protostars should be observed at milli–arcsecond resolution to better characterize the outflow structure close to the protostar, and simulations must be developed and tested specifically for the conditions expected near luminous protostars.

References and Notes

1. A. Königl, R. E. Pudritz, in *Protostars and Planets IV*, V. Mannings, A. Boss, S. Russell, Eds. (Univ. of Arizona Press, Tucson, 2000), pp. 759–787.
2. F. H. Shu, J. R. Najita, H. Shang, Z.-Y. Li, in *Protostars and Planets IV*, V. Mannings, A. Boss, S. Russell, Eds. (Univ. of Arizona Press, Tucson, 2000), pp. 789–813.
3. N. Calvet, L. Hartmann, S. E. Strom, in *Protostars and Planets IV*, V. Mannings, A. Boss, S. Russell, Eds. (Univ. of Arizona Press, Tucson, 2000), pp. 377–399.
4. D. J. Hollenbach, H. W. Yorke, D. Johnstone, in *Protostars and Planets IV*, V. Mannings, A. Boss, S. Russell, Eds. (Univ. of Arizona Press, Tucson, 2000), pp. 401–428.
5. J. R. Najita, S. Edwards, G. Basri, J. Carr, in *Protostars and Planets IV*, V. Mannings, A. Boss, S. Russell, Eds. (Univ. of Arizona Press, Tucson, 2000), pp. 457–483.
6. D. S. Shepherd, E. Churchwell, *Astrophys. J.* **472**, 225 (1996).
7. D. S. Shepherd, A. M. Watson, A. I. Sargent, E. Churchwell, *Astrophys. J.* **507**, 861 (1998).
8. R. L. Snell, R. L. Dickman, Y.-L. Huang, *Astrophys. J.* **352**, 139 (1990).
9. K-W. Hodapp, *Astrophys. J. Suppl. Ser.* **94**, 615 (1994).
10. D. S. Shepherd, S. Kurtz, *Astrophys. J.* **523**, 690 (1999).
11. D. Devine, J. Bally, B. Reipurth, D. Shepherd, A. M. Watson, *Astron. J.* **117**, 2919 (1999).
12. C. Codella, M. Felli, V. Natale, *Astron. Astrophys.* **311**, 971 (1996).
13. F. H. Shu, H. Shang, in *Herbig-Haro Flows and the Birth of Low Mass Stars, IAU Symposium 182*, B. Reipurth, C. Bertout, Eds. (Kluwer, Dordrecht, Netherlands, 1997), pp. 225–239.
14. R. E. Pudritz, R. Ouyed, in *Herbig-Haro Flows and the Birth of Low Mass Stars, IAU Symposium 182*, B. Reipurth, C. Bertout, Eds. (Kluwer, Dordrecht, Netherlands, 1997), pp. 259–274.
15. S. Cabrit, A. Raga, F. Gueth, in *Herbig-Haro Flows and the Birth of Low Mass Stars, IAU Symposium 182*, B. Reipurth, C. Bertout, Eds. (Kluwer, Dordrecht, Netherlands, 1997), pp. 163–180.
16. R. Beresford *et al.*, in preparation.
17. A fast-switching cycle time of 140 s provided an on-source efficiency of 35%, which resulted in an on-source time of 1.6 hours. The quasar J0539+145 was used as a phase calibrator, and quasars J0713+438 and 3C286 were used as flux calibrators. The estimated uncertainty of the flux calibration is ~10%. Calibration was performed with the AIPS data reduction package. Images were produced with the MIRIAD software package (*50*). The data were imaged with ROBUST weighting to provide an optimal compromise between resolution and noise minimization. The resulting image was deconvolved with a CLEAN-based algorithm.
18. J. E. Pringle, *Mon. Not. R. Astron. Soc.* **258**, 811 (1992).
19. C. Fendt, H. Zinnecker, *Astron. Astrophys.* **334**, 750 (1998).
20. C. Terquem, J. Eislöffel, J. C. B. Papaloizou, R. P. Nelson, *Astrophys. J. Lett.* **512**, L131 (1999).
21. D. S. Shepherd, K. C. Yu, J. Bally, L. Testi, *Astrophys. J.* **535**, 833 (2000).
22. F. Motte, P. André, R. Neri, *Astron. Astrophys.* **336**, 150 (1998).
23. R. H. Hildebrand, *Q. J. R. Astron. Soc.* **24**, 267 (1983).
24. C. Kramer *et al.*, *Astron. Astrophys.* **329**, L33 (1998).
25. K. R. Bell, P. M. Cassen, H. H. Klahr, Th. Henning, *Astrophys. J.* **486**, 372 (1997).
26. J. B. Pollack *et al.*, *Astrophys. J.* **421**, 615 (1994).
27. L. Testi, A. I. Sargent, *Astrophys. J.* **508**, L91 (1998).
28. N. Panagia, *Astron. J.* **78**, 929 (1973).
29. R. I. Thompson, *Astrophys. J.* **283**, 165 (1984).
30. E. Churchwell, in *The Physics of Star Formation and Early Stellar Evolution*, C. J. Lada, W. D. Kylafis, Eds. (Kluwer, Dordrecht, Netherlands, 1991), pp. 221–261.
31. P. Saraceno, P. Andre, C. Ceccarelli, M. Griffin, S. Molinari, *Astron. Astrophys.* **309**, 827 (1996).
32. S. Guilloteau, A. Dutrey, M. Simon, *Astron. Astrophys.* **348**, 570 (1999).
33. R. D. Mathieu, A. M. Ghez, E. L. N. Jensen, M. Simon, in *Protostars and Planets IV*, V. Mannings, A. Boss, S. Russell, Eds. (Univ. of Arizona Press, Tucson, 2000), pp. 703–730.
34. J.-M. Huré, *Astron. Astrophys.* **358**, 378 (2000).
35. To illustrate this point, consider a uniform 1000-AU-diameter circumbinary torus that is inclined 70° with respect to the line of sight. With an average disk temperature of 10 K, the disk could have a mass as high as 500 $M_\odot$ and still be below our 1σ noise level at 43 GHz. However, it should be detectable in a high-density tracer such as $C^{18}O$. In fact, a velocity gradient is detected across a 120 $M_\odot$ $C^{18}O$ core (*10*). The measured velocities are consistent with rotation in a flattened structure,

but the resolution of ~2″ was not sufficient to determine whether the $C^{18}O$ emission was confined to a circumbinary structure, the remnant cloud core, or a combination of the two.
36. B. Reipurth, *Astron. J.* **120**, 3177 (2000).
37. E. L. N. Jensen, R. D. Mathieu, G. A. Fuller, *Astrophys. J. Lett.* **429**, L29 (1994).
38. S. H. Lubow, P. Artymowicz, in *Protostars and Planets IV*, V. Mannings, A. Boss, S. Russell, Eds. (Univ. of Arizona Press, Tucson, 2000), pp. 731–755.
39. A. I. Sargent, in *Disks and Outflows Around Young Stars*, S. V. W. Beckwith, A. Natta, J. Staude, Eds. (Springer-Verlag, Berlin, 1995), pp. 1–17.
40. G. Laughlin, P. Bodenheimer, *Astrophys. J.* **436**, 335 (1994).
41. H. W. Yorke, P. Bodenheimer, G. Laughlin, *Astrophys. J.* **443**, 199 (1995).
42. J. M. Stone, C. F. Gammie, S. A. Balbus, J. F. Hawley, in *Protostars and Planets IV*, V. Mannings, A. Boss, S. Russell, Eds. (Univ. of Arizona Press, Tucson, 2000), pp. 589–611.
43. R. Cesaroni *et al.*, *Astron. Astrophys.* **345**, 949 (1999).
44. L. Moscadelli, R. Cesaroni, M. J. Rioja, *Astron. Astrophys.* **360**, 663 (2000).
45. L. F. Rodríguez *et al.*, *Astrophys. J.* **430**, L65 (1994).
46. G. Narayanan, C. K. Walker, *Astrophys. J.* **466**, 844 (1996).
47. J. Martí, L. F. Rodríguez, J. M. Torrelles, *Astron. Astrophys.* **345**, L5 (1999).
48. J. Eislöffel, R. Mundt, T. P. Ray, L. F. Rodríguez, in *Protostars and Planets IV*, V. Mannings, A. Boss, S. Russell, Eds. (Univ. of Arizona Press, Tucson, 2000), pp. 815–840.
49. R. Ouyed, R. E. Pudritz, *Mon. Not. R. Astron. Soc.* **309**, 233 (1999).
50. R. J. Sault, P. J. Teuben, M. C. H. Wright, in *Astronomical Data Analysis Software and Systems IV*, vol. 77 of *PASP Conference Series*, R. A. Shaw, H. E. Payne, J. J. E. Hayes, Eds. (Astronomical Society of the Pacific, San Francisco, 1995), pp. 433–437.
51. The National Radio Astronomy Observatory (NRAO) is a facility of the National Science Foundation operated under cooperative agreement by Associated Universities, Inc. (AUI). We would like to thank G. Chavez and R. Hayward for building and optimizing the 7-mm receivers at the VLA. Without their efforts, observations of this caliber would not have been possible. We thank the entire team of NRAO staff working on the VLA-PT link project, in particular, R. Beresford and K. Sowinski for developing and supporting the VLA-PT link. Finally, we are grateful to the NSF and AUI for funding the PT link project and to Western New Mexico Telephone Company for the use of the fiber.

1 February 2001; accepted 11 April 2001

Spatially Resolved Spin-Injection Probability for Gallium Arsenide

V. P. LaBella,[1*] D. W. Bullock,[1] Z. Ding,[1] C. Emery,[1] A. Venkatesan,[1] W. F. Oliver,[1] G. J. Salamo,[1] P. M. Thibado,[1] M. Mortazavi[2]

We report a large spin-polarized current injection from a ferromagnetic metal into a nonferromagnetic semiconductor, at a temperature of 100 Kelvin. The modification of the spin-injection process by a nanoscale step edge was observed. On flat gallium arsenide [GaAs(110)] terraces, the injection efficiency was 92%, whereas in a 10-nanometer-wide region around a [$\bar{1}$11]-oriented step the injection efficiency is reduced by a factor of 6. Alternatively, the spin-relaxation lifetime was reduced by a factor of 12. This reduction is associated with the metallic nature of the step edge. This study advances the realization of using both the charge and spin of the electron in future semiconductor devices.

The ability to exploit the spin of the electron in semiconductor devices has the potential to revolutionize the electronics industry (*1–3*). The realization of "spintronic" devices is growing nearer as sources for spin-polarized electrons have become available in both ferromagnetic metals and ferromagnetic semiconductors (*4*, *5*). In addition, polarized electrons can move up to 100 μm in gallium arsenide (GaAs) without losing their polarization, so that coherent transport through the active region of a device structure is feasible (*6*). However, one of the most difficult challenges in creating "spintronic" devices is the ability to transfer the polarized electrons from a ferromagnetic material into a nonferromagnetic semiconductor without substantially degrading the polarization. For example, ferromagnetic metal contacts give spin-injection efficiencies of only a few percent at 4 K (*7*, *8*). Injection efficiencies using ferromagnetic semiconductors as contacts are as high as 90%; however, this is also only at 4 K (*9–11*). From the success of the all-semiconductor approach, it is thought that an epitaxial lattice-matched system is required for efficient spin injection. However, recent findings have demonstrated high injection efficiencies even with large lattice mismatches (*11*). These results have sparked renewed interest in determining the origin of spin-flip scattering mechanisms on a nanometer-length scale.

Tunneling-induced luminescence microscopy (TILM) makes it possible to correlate nanoscale features with their optical properties by injecting electrons and measuring the recombination luminescence (*12–14*). This technique cannot correlate the spin of the electron to any properties of the sample. However, with a spin-polarized scanning tunneling spectroscopy (STS) technique that incorporates a ferromagnetic metal tip, a net polarization in the recombination luminescence can be measured and related to the polarization state of the electrons at the time of recombination (*15*, *16*). This type of measurement has shown that vacuum tunneling preserves the spin-polarization properties of the electrons. The addition of the ability to correlate a surface feature seen in the topography of a scanning tunneling microscopy (STM) image with the degree of spinflip scattering is needed to better understand what affects the spin-injection process. For example, simultaneous imaging and spin-injection probability mapping of a surface would allow one to uncover what features and what mechanisms disrupt the spin-injection process.

We demonstrate that a large spin-polarized (~92%) current can be injected into GaAs at high temperatures (100 K). In addition, [$\bar{1}$11]-oriented steps are found to substantially decrease the injection efficiency (by a factor of 6). This observation is correlated to the density of midgap states.

A 100% spin-polarized STM tip was used as the electron source to locally inject polarized electrons into a p-type GaAs(110) surface while simultaneously measuring the polarization of the recombination luminescence. This spin-polarized TILM is similar to TILM, with the additional features that the injected electrons are spin polarized and the polarization state of the recombination luminescence is measured (*12–14*).

A polarized electron current was generated from a ferromagnetic single-crystal Ni<110> wire. Along the <110> direction in Ni, the density of spin-down states at the Fermi level is nonzero whereas the density of spin-up states is zero (*17*). Therefore, only the spin-down electrons contribute to conduction. The direction of the magnetization of the tips was determined to lie along the long axis of the wire as measured by a superconducting quantum interference device magnetometer. In addition, the wire was determined to have a remnant field of 0.3 Oe and a coercive field of 30 Oe; for additional experimental details, see (*18*).

Electrons injected into the empty conduction band states of GaAs eventually recombine across the 1.49-eV (100 K) band gap, emitting light, which is collected using a biconvex lens having an f-number of 1.0. The lens is mounted in situ and positioned 12.7

[1]Department of Physics, University of Arkansas, Fayetteville, AR 72701, USA. [2]Department of Physics, University of Arkansas, Pine Bluff, AR 71601, USA.

*To whom correspondence should be addressed. E-mail: vlabella@uark.edu